

Saturation of magnetised plasma turbulence by propagating zonal flows

R. Nies^{1,2}, F. Parra^{1,2}, M. Barnes³, N. Mandell², and W. Dorland⁴

¹*Department of Astrophysical Sciences, Princeton University, Princeton, NJ 08543, USA*

²*Princeton Plasma Physics Laboratory, Princeton, NJ 08540, USA*

³*Rudolf Peierls Centre for Theoretical Physics, University of Oxford, Oxford OX1 3NP, United Kingdom*

⁴*Department of Physics, University of Maryland, College Park, MD 20742, USA*

(Dated: September 5, 2024)

Strongly driven ion-scale turbulence in tokamak plasmas is shown to be regulated by a new propagating zonal flow mode, the toroidal secondary, which is nonlinearly supported by the turbulence. The mode grows and propagates due to the combined effects of zonal flow shearing and advection by the magnetic drift. Above a threshold in the turbulence level, small-scale toroidal secondary modes become unstable and shear apart turbulent eddies, forcing the turbulence level to remain near the threshold. By including the new zonal flow physics into a theory of turbulence saturation based on the critical balance conjecture, scaling laws for the turbulent heat flux, fluctuation spectra, and zonal flow amplitude are derived and shown to be satisfied in nonlinear gyrokinetic simulations.

Introduction.— Efforts to achieve the high temperatures required for thermonuclear fusion in magnetically confined plasmas are stymied by the large heat flux caused by turbulent mixing. The turbulent fluctuations are driven by micro-instabilities, most notably the ion temperature gradient (ITG) instability [1]. The saturation level of such ion-scale modes crucially depends on zonal flows (ZFs) [2, 3], flow bands that are nonlinearly generated by the turbulence [4] and can shear apart turbulent eddies. In toroidal plasmas, the linear ZF physics allows for stationary ZFs [5, 6] and fast oscillating geodesic acoustic modes (GAMs) [7, 8].

In this Letter, we show that strongly driven tokamak ITG turbulence exhibits a new small-scale propagating ZF mode, the toroidal secondary. We elucidate the physics of the new mode, and demonstrate its relevance to turbulence saturation. We then show how the application of the critical balance conjecture to ITG turbulence [9] must be altered to account for the role of the toroidal secondary. The revised theory leads to new scalings of the fluctuation amplitude and length scales, which are found to be in agreement with nonlinear gyrokinetic simulations and with past experimental observations [10].

Tokamak turbulence.— To avoid fast parallel losses, the magnetic field of tokamaks is made to lie on nested toroidal ‘flux surfaces’. The plasma quickly reaches local thermodynamic equilibrium and is thus approximately Maxwellian, with the density n_s and temperature T_s of each species s uniform on flux surfaces. The resulting radial gradients between the hot dense core and the cold dilute edge drive turbulent fluctuations which cause transport across flux surfaces. These fluctuations are slow compared to the Larmor gyration frequency $\Omega_s = e_s B / m_s$, with the particle mass m_s and charge e_s , and B the magnetic field strength. The fast gyratory motion may thus be averaged over, and the turbulence may be modelled using gyrokinetics [11], which describes rings of charge centered on the gyrocentre position \mathbf{R} , shifted from the particle position \mathbf{r} by the gyroradius

vector.

Moreover, in the tokamak core, the fluctuations in the distribution function f_s are generally small compared to the Maxwellian background F_{Ms} , i.e., $\delta f_s = f_s - F_{Ms} \ll F_{Ms}$, and they are highly anisotropic. Indeed, the typical turbulence length scales parallel to the magnetic field are of the order of the tokamak size, as measured e.g. by the major radius R , while in the perpendicular direction they are on the much smaller gyro-radius scale $\rho_s = v_{Ts} / \Omega_s \ll R$, with the thermal speed $v_{Ts} = (2T_s / m_s)^{1/2}$. The fluctuations may thus be described locally in a flux-tube domain, as shown in Fig. 3a, taking the magnetic field geometry to only vary along the field line on a chosen flux surface denoted by r_0 . Here, we assume the tokamak flux surfaces to have circular cross-section, and we choose the radial coordinate to be $x = r - r_0$, with r the radial distance from the magnetic axis. As x labels flux surfaces, its gradient is parallel to the density and temperature gradients. The binormal coordinate y and the parallel coordinate θ determine the position within a flux-surface: y , like x , is perpendicular to \mathbf{B} , whereas θ gives the location along \mathbf{B} . Then, the flux-surface average $\langle A \rangle_{y\theta}$ of a given quantity A is given by its average in y and θ , the latter including the Jacobian $1 / \mathbf{B} \cdot \nabla \theta$. Finally, we also define the zonal and nonzonal components of A through $A^Z \equiv \langle A \rangle_y = A - A^{NZ}$.

In this Letter, we consider electrostatic and collisionless ion-scale fluctuations, for a single ion species with charge $e_i = Z_i e$. The gyrokinetic equation may be written in terms of the non-adiabatic part of the perturbed ion distribution function $h_i = \delta f_i + F_{Mi} e_i \varphi / T_i$, using the particle energy and magnetic moment as velocity-space coordinates,

$$\begin{aligned} \partial_t (h_i - F_{Mi} e_i \bar{\varphi} / T_i) + \left(v_{\parallel} \hat{\mathbf{b}} + \tilde{\mathbf{v}}_M \right) \cdot \nabla h_i \\ + \bar{\mathbf{v}}_E \cdot \nabla (F_{Mi} + h_i) = 0, \end{aligned} \quad (1)$$

where the fluctuating electrostatic potential φ is self-

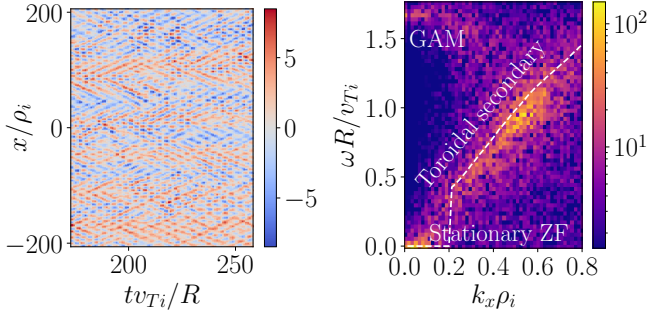


FIG. 1: Normalised zonal flow velocity $\langle v_E^Z/v_{Ti} \rangle_\theta R/\rho_i$ from saturated ITG turbulence far from marginality ($q = 2.8$, $R/L_T = 10.4$) in real space (left), and the absolute value of its Fourier amplitude (right). The oscillation frequency of the secondary mode (dashed line) reproduces the frequency in the nonlinear simulation.

consistently determined by quasineutrality

$$\frac{T_i}{e_i n_i} \int d^3v \bar{h}_i = \tau (\bar{\varphi} - \langle \varphi \rangle_{y\theta}) + \varphi, \quad (2)$$

with $\tau = T_i/Z_i T_e$ and $\hat{\mathbf{b}} = \mathbf{B}/B$. The overlines indicate gyro-averages, with the $\bar{\varphi}$ average taken at fixed gyrocentre position \mathbf{R} , and \bar{h}_i at fixed real space position \mathbf{r} . The electrons were assumed in (2) to respond adiabatically only to potential variations within flux surfaces $\varphi - \langle \varphi \rangle_{y\theta}$, as they cannot move radially due to their small gyroradii. The gyrokinetic equation includes advection by the magnetic drift $\tilde{\mathbf{v}}_M$ and by the gyro-averaged $\mathbf{E} \times \mathbf{B}$ -drift $\bar{\mathbf{v}}_E = \hat{\mathbf{b}} \times \nabla \bar{\varphi}/B$, with the latter determining the time-and-volume-averaged radial heat flux $\langle Q \rangle_{txy\theta}$, with

$$Q = \frac{1}{\langle |\nabla x| \rangle_\theta} \int d^3v \frac{m_i v^2}{2} \bar{h}_i \mathbf{v}_E \cdot \nabla x, \quad (3)$$

which is of primary interest to ascertain the level of transport caused by turbulent fluctuations.

Propagating zonal flows.— In gyrokinetic simulations of strongly driven ITG turbulence, ZF activity is apparent at multiple scales, see Fig.1, showing large-scale stationary ZFs and small-scale propagating ZFs. The corresponding Fourier spectrum in Fig.1 exhibits stationary ZFs and GAMs at large radial scales $k_x \rho_i \sim 0.1$, and a new propagating ZF mode, the toroidal secondary. It is predominant at smaller scales $k_x \rho_i \sim 0.5$, and has a frequency $\omega \sim k_x v_{Mx}$ set by the radial magnetic drift velocity $v_{Mx} \equiv \rho_i v_{Ti}/R$, defined such that

$$\tilde{v}_{Mx} = v_{Mx} \sin \theta \frac{v_{\parallel}^2 + v_{\perp}^2/2}{v_{Ti}^2} \quad (4)$$

in a large aspect-ratio tokamak of circular cross-section.

Unless specified otherwise, the gyrokinetic simulations presented in this Letter are performed using **stella**

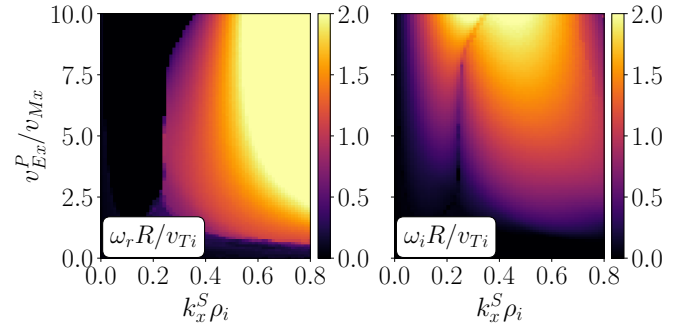


FIG. 2: Oscillation frequency (left) and growth rate (right) of secondary mode with radial wavenumber k_x^S due to a primary streamer mode with varying amplitude, measured by $v_{Ex}^P = \langle v_{Ex}^2 \rangle_{y\theta}^{1/2}$. The primary is a linear ITG mode with binormal wavenumber $k_y \rho_i = 0.05$, at $q = 1.4$ and $R/L_T = 13.9$.

[12]. The simulations model a flux surface at half-radius $r_0 = a/2$ of the Cyclone Base Case, a tokamak with flux surfaces of circular cross-section and inverse aspect ratio $R/a = 2.8$, where a is the tokamak minor radius. The safety factor q gives the magnetic field line pitch and sets the connection length $L_{\parallel} = qR$, with $2\pi L_{\parallel}$ the distance along the field line corresponding to one poloidal turn. The safety factor is varied between simulations, as is the ion temperature gradient $R/L_T \equiv -R d \ln T_i / dr$, while the density gradient and other quantities are held fixed at the usual Cyclone Base Case values. These are listed in the Supplementary Material, alongside the numerical parameters used in all simulations.

Compared to the small-scale, fast-oscillating toroidal secondary, the background turbulence has long radial wavelengths and evolves slowly in time, as will be shown explicitly below. The physics of the toroidal secondary may therefore be understood by considering a secondary mode growing and propagating over a background stationary ($\partial_t = 0$) streamer ($k_x = 0$) mode, referred to as the primary mode and taken to be representative of the turbulence. This secondary model was originally considered by [4], where the magnetic drift and parallel streaming in (1) were ignored, leading to a purely growing mode. As shown in Fig. 2, gyrokinetic simulations of the secondary additionally exhibit the small-scale oscillating ZFs observed in the fully nonlinear gyrokinetic simulations, and a purely growing mode is observed only at large primary drive or long ZF wavelengths. We note that dispersion relations for the various modes may be derived analytically using the secondary formalism. These will be presented in future work, as we here focus on the phenomenology and physical mechanism of the toroidal secondary, and its effect on the turbulence.

To understand the mechanism for ZF drive and propagation, let us consider the vorticity equation at long

perpendicular wavelengths,

$$n_i \partial_t \langle \rho_i |\nabla x| \partial_x v_E^Z \rangle_\theta = \quad (5)$$

$$v_{Ti} \partial_x \left\langle \int d^3v \left((v_\perp^2 / 2\Omega_i^2) \nabla x \cdot \nabla \mathbf{v}_E \cdot \nabla h_i + \tilde{v}_{Mx} h_i \right) \right\rangle_{y\theta},$$

which is derived from the time-derivative and flux-surface average of (2). The vorticity equation describes the evolution of the ZF velocity $v_E^Z = |\nabla x| \partial_x \langle \varphi \rangle_y / B$ due to nonlinear Reynolds and diamagnetic stresses, and due to the \tilde{v}_{Mx} -induced Stringer-Winsor (SW) force [7, 13–15], which is dominant for the toroidal secondary. The SW force results from up-down asymmetries in $(P + e_i n_i \varphi)^Z$, with the fluctuating pressure

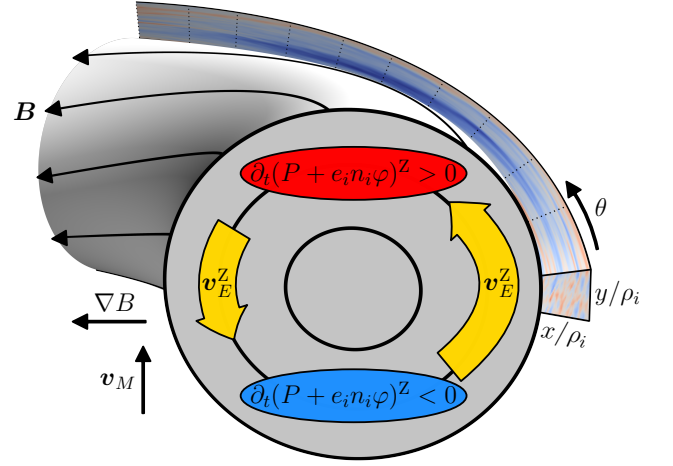
$$P \equiv \int d^3v \frac{m_i}{2} \left(v_\parallel^2 + \frac{v_\perp^2}{2} \right) \delta f_i, \quad (6)$$

as the magnetic drift points radially outward above the tokamak midplane and inward below it, reflected in the $\sin \theta$ of (4) and sketched in Fig. 3a.

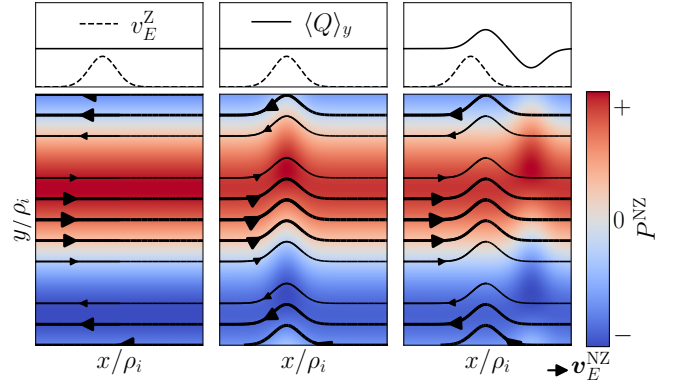
As illustrated in Fig. 3a, the $(P + e_i n_i \varphi)^Z$ asymmetry can be generated by the ZF itself, through the compression induced by the varying ZF velocity $v_E^Z \propto 1/B$ between the tokamak outboard and inboard sides. In the case of the toroidal secondary, up-down asymmetry in P^Z is also generated nonlinearly, due to the radial magnetic drift (4) advecting eddies sheared by the zonal flow, as explained in Fig. 3b. The $(P + e_i n_i \varphi)^Z$ asymmetry is generated on flux surfaces neighbouring the ZF perturbation, causing the mode to propagate and also grow provided the up-down asymmetry is sufficiently large. At long radial wavelengths, the ZF inertia in (5) (the term with ∂_t) becomes negligible, such that the two mechanisms of $(P + e_i n_i \varphi)^Z$ asymmetry generation described in Fig. 3 must cancel each other. Toroidal secondary modes therefore oscillate more slowly than GAMs (see Fig. 1), for which the compressibility-induced SW force is balanced by the ZF inertia. We note that the toroidal secondary mechanism is distinct from that of [15, 16], who consider the pressure asymmetry generation due to a combination of ZF shearing and the effect of magnetic shear \hat{s} .

The physical picture outlined above did not include the effects of parallel streaming, which acts to short-circuit the up-down $(P + e_i n_i \varphi)^Z$ asymmetries. Therefore, the toroidal secondary is only found at short radial wavelengths, where $\omega \sim k_x v_{Mx} \gtrsim v_\parallel \hat{\mathbf{b}} \cdot \nabla \sim v_{Ti} / qR$. At longer radial wavelengths, the ZFs do not oscillate, as seen in the gyrokinetic simulations of the secondary (Fig. 2) or of the nonlinear turbulence (Fig. 1). Furthermore, to avoid kinetic damping by the magnetic drift, the toroidal secondary mode requires a sufficiently large primary drive $v_{Ex} \gtrsim v_{Mx}$ to become unstable, as shown in Fig. 2. Finally, the toroidal secondary is stabilised by finite Larmor radius effects, such that the growth rate peaks at $k_x \rho_i \sim 0.5$ in Fig. 2, explaining the prominent ZFs at this scale in fully nonlinear simulations (Fig. 1).

Zonal flows and turbulence saturation.— To ascertain the role of the various zonal flow modes in setting the



(a) Tokamak geometry and coordinate conventions for flux-tube turbulence simulations, and illustration of $(P + e_i n_i \varphi)^Z$ asymmetry generation through ZF compressibility.



(b) Generation of P^Z asymmetry from nonlinear heat flux, illustrated above the tokamak midplane where $\tilde{v}_{Mx} > 0$: starting from a streamer mode (left), the v_E^Z perturbation shears the nonzonal $\mathbf{E} \times \mathbf{B}$ -flow and pressure contours equally, leaving the heat flux $\langle Q \rangle_y \propto \langle v_E^Z P^{NZ} \rangle_y$ (3) unchanged (middle). Including the advection by the velocity-dependent radial magnetic drift \tilde{v}_{Mx} (4), a relative displacement between the nonzonal $\mathbf{E} \times \mathbf{B}$ -flow and pressure fluctuations ensues, leading to a radial modulation of the nonlinear heat flux $\langle Q \rangle_y$ (right). This mechanism is reversed below the midplane where $\tilde{v}_{Mx} < 0$, such that there is up-down asymmetry in the heat flux and thence also in P^Z .

FIG. 3: Mechanisms for generation of $(P + e_i n_i \varphi)^Z$ up-down asymmetry contributing to the toroidal secondary.

turbulence saturation level, we consider the energy transfer in k_x caused by ZFs at different scales. Let us define the low-pass-filtered distribution

$$h_{i,Kx} \equiv \int_{-Kx}^{Kx} dk_x \hat{h}_i(k_x) e^{ik_x X}, \quad (7)$$

where the Fourier modes $\hat{h}_i(k_x)$ are normalised such that

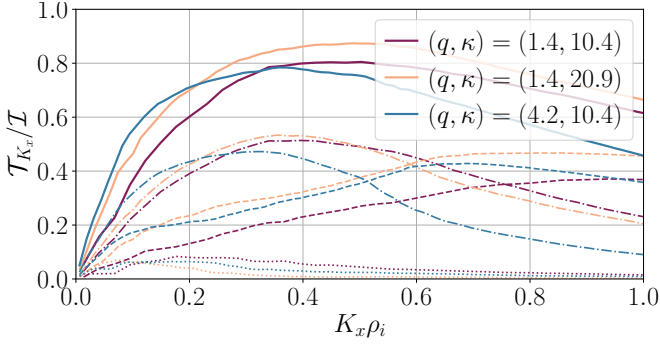


FIG. 4: Energy transfer rate \mathcal{T}_{K_x} (10) normalised by the total injection rate $\mathcal{I} = \lim_{K_x \rightarrow \infty} \mathcal{I}_{K_x} = \langle Q \rangle_{xy\theta} / L_T$ in nonlinear gyrokinetic simulations. The contributions to the transfer rate (solid line) are obtained by decomposing \mathbf{v}_E in (10) into its nonzonal (dashed), small-scale $|k_x \rho_i| > 0.3$ zonal (dash-dotted), and large-scale $|k_x \rho_i| \leq 0.3$ zonal (dotted) components.

$h_i = \lim_{K_x \rightarrow \infty} h_{i,K_x}$. Then, the low-pass filtered gyrokinetic free-energy

$$\mathcal{E}_{K_x} \equiv \sum_s T_s \left\langle \int d^3v \frac{(\delta f_{s,K_x})^2}{2F_{Ms}} \right\rangle_{xy\theta} \quad (8)$$

may be shown to evolve as

$$\partial_t \mathcal{E}_{K_x} + \mathcal{T}_{K_x} = \mathcal{I}_{K_x} - \mathcal{D}_{K_x}, \quad (9)$$

with the energy transfer rate

$$\mathcal{T}_{K_x} = \left\langle T_i \int d^3v \frac{h_{i,K_x}}{F_{Mi}} \mathbf{v}_E \cdot \nabla h_i \right\rangle_{xy\theta}, \quad (10)$$

the injection rate

$$\mathcal{I}_{K_x} = L_T^{-1} \left\langle \int d^3v \frac{m_i v^2}{2} \overline{h_{i,K_x}} \mathbf{v}_E \cdot \nabla x \right\rangle_{xy\theta}, \quad (11)$$

and a dissipation rate \mathcal{D}_{K_x} , e.g. from collisions or numerical dissipation.

In Fig. 4, the small-scale ZFs are shown to play a crucial role in transferring energy from large to small radial scales, as they are the largest contributors to \mathcal{T}_{K_x} at radial wavenumbers larger than the toroidal secondary scale $K_x \rho_i \sim 0.5 - 0.7$; for larger K_x the nonzonal contribution is dominant. The contribution to \mathcal{T}_{K_x} from the large-scale ZFs is subdominant, though we note that numerical experiments artificially removing the ZFs at small k_x were found to alter the turbulence saturation level.

Turbulence scaling laws.— We now consider how the toroidal secondary modes may be incorporated in a theory of turbulence saturation. Strongly driven ITG turbulence in tokamaks has previously been modelled [9] using the critical balance conjecture [17], which posits the nonlinear transfer rate ω_{NL} and parallel propagation rate ω_{\parallel}

of the saturated turbulence to be of the same order: at every scale, $\omega_{NL} \sim v_{Ex}/l_x \sim \omega_{\parallel} \sim v_{Ti}/l_{\parallel}$, with the rates estimated from (1). Here, l_x, l_y, l_{\parallel} are the radial, binormal, and parallel length scales of the turbulence. At the turbulence outer scale, denoted by ‘o’ superscripts, ω_{NL} must also balance the energy injection rate ω_{\star}^T , such that $\omega_{NL}^o \sim \omega_{\star}^{T,o} \sim (v_{Ti}/L_T) \rho_i / l_y^o$. Furthermore, the parallel outer length scale in a tokamak is assumed to be the connection length $l_{\parallel}^o \sim L_{\parallel} = qR$.

In the original theory of [9], the turbulent eddies were assumed to be isotropic in the directions perpendicular to the magnetic field, i.e., $l_x \sim l_y$. In fact, the turbulence is anisotropic at the outer scale due to the small-scale ZFs, with the turbulence level regulated to be near the marginal stability threshold of the toroidal secondary, $v_{Ex} \sim v_{Mx}$ (see Fig. 2). This corresponds to a grand critical balance at the outer scale, $\omega_{NL}^o \sim \omega_{\parallel}^o \sim \omega_{\star}^{T,o} \sim \omega_{Mx}^o$ with $\omega_{Mx} \sim v_{Mx}/l_x$, in agreement with previously unexplained experimental observations [10].

Grand critical balance leads to the following scalings for the turbulence length scales, amplitude, and heat flux at the outer scale:

$$\frac{l_y^o}{\rho_i} \sim \frac{qR}{L_T}, \frac{l_x^o}{\rho_i} \sim q, \frac{e_i \varphi^o}{T_i \rho_i} \frac{R}{\rho_i} \sim \frac{qR}{L_T}, \frac{\langle Q \rangle_{txy\theta}}{Q_{gB}} \sim \frac{qR}{L_T}, \quad (12)$$

with the gyro-Bohm heat flux $Q_{gB} = n_i T_i v_{Ti} (\rho_i/R)^2$. Notably, the heat flux is predicted to scale only linearly with the background temperature gradient, instead of the cubic scaling predicted for perpendicularly isotropic eddies [9][18]. This revised heat flux scaling is satisfied in gyrokinetic simulations, as shown in Fig. 5a. Furthermore, we verify the grand critical balance scalings for the turbulence amplitude and outer scale by considering the fluctuation spectra, as shown in Figs. 5c and 5d.

Finally, we note that, as q is increased, there is a clear scale separation between the turbulence outer scale $k_x \rho_i \sim 1/q$, and the toroidal secondary scale $k_x \rho_i \sim 0.5$, where the turbulence spectrum exhibits only a small local peak, see Fig. 5d. Therefore, the grand critical balance scalings (12) also justify the secondary model considered in Figs. 2 and 3 to describe the toroidal secondary mode, as the turbulence evolves over long spatio-temporal scales $k_x \rho_i \sim 1/q$ and $\omega_{NL}^o \sim v_{Ti}/qR$ compared to the toroidal secondary’s high wavenumber $k_x \rho_i \sim 1$ and frequency $\omega^{ZF} \sim v_{Ti}/R$. Due to the fast ZF oscillation, the shearing of turbulent eddies is not coherent, and must be modelled diffusively instead. To affect turbulence saturation, the ZFs must cause diffusion over an eddy length scale l_y^o in a nonlinear time, i.e., $(l_y^o)^2 \sim D/\omega_{NL}^o$, where $D \sim (v_E^Z)^2/\omega^{ZF}$ is the diffusivity due to ZFs. Using (12), the zonal flow energy

$$E^{ZF} \equiv \frac{e_i^2}{2n_i T_i} \left\langle \int d^3v \varphi^Z \left(\varphi^Z - \overline{\varphi^Z} \right) F_M \right\rangle_{tx\theta} \quad (13)$$

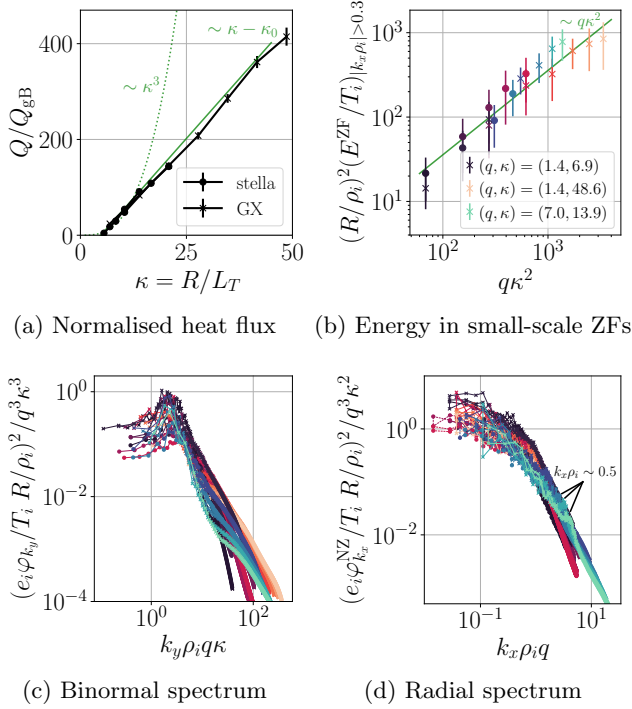


FIG. 5: Verification of grand critical balance scalings (12) and (14) in nonlinear gyrokinetic simulations using the codes *stella* [9] (circles) and *GX* [19, 20] (crosses). The nonzonal potential fluctuation spectra in (c-d) are rescaled according to the grand critical balance prediction at the outer scale (12). In (b-d), the cold colors (black→blue→cyan) correspond to the q scan, while the warm colors (black→red→yellow) correspond to the κ scan. The error bars in (b) correspond to the standard deviation in time of the zonal flow energy. In (d), small local peaks at the toroidal secondary scale $k_x \rho_i \sim 0.5$ are highlighted.

is thus predicted to scale as

$$\frac{E^{ZF}}{T_i} \approx \left\langle \left(\frac{v_E^Z}{v_{Ti}} \right)^2 \right\rangle_{tx\theta} \sim q \left(\frac{R}{L_T} \right)^2 \left(\frac{\rho_i}{R} \right)^2. \quad (14)$$

Here, the quantity $\overline{\varphi^Z}$ in (13) corresponds to two successive gyro-averages, first at fixed \mathbf{R} and then at fixed \mathbf{r} and were approximated in the long-wavelength limit $k_{\perp} \rho_i \ll 1$ in (14). As shown in Fig. 5b, the predicted ZF

scaling (14) is well satisfied by the small-scale toroidal secondary modes in gyrokinetic simulations.

Discussion.— In this Letter, we have presented the toroidal secondary, a new mode which leads to small-scale propagating zonal flows in nonlinear gyrokinetic simulations of ITG turbulence (Fig. 1). The toroidal secondary regulates the turbulence saturation level to be near the threshold turbulence amplitude $v_{Ex} \sim v_{Mx}$ for which the toroidal secondary mode becomes unstable (Fig. 2). As a consequence, the turbulence follows the grand critical balance previously observed experimentally [10], leading to turbulence scaling laws (12) satisfied in gyrokinetic simulations (Fig. 5).

We note that toroidal secondary modes resulting from electron-scale turbulence could differ considerably in character from those presented in this Letter, as the ZF inertia will play a more important role. For ion scale modes, the ZF inertia does not contribute significantly to the toroidal secondary mechanism due to the modified adiabatic electron response in (2), which leads to a small ZF inertia at long wavelengths, see (5).

The toroidal secondary modes shown in Fig. 1 are reminiscent of the avalanches previously observed in gyrokinetic simulations [e.g. 21, 22], whose physical mechanism remains debated. Recent efforts [23] to model the avalanches have considered the coupling of zonal flows with both the turbulence and with toroidal geometric effects, though nonlinear fluxes were neglected, precluding the toroidal secondary modes presented here (see Fig. 3b). From Fig. 1, the toroidal secondary is seen to have a typical propagation velocity $\sim 2v_{Ti}\rho_i/R$, comparable to previously reported avalanche propagation speeds [22, 24]. Furthermore, the turbulence amplitude threshold required to destabilise the toroidal secondary could explain the sandpile-like behaviour associated with avalanches.

This work was supported by U.S. DOE DE-AC02-09CH11466 and DE-FG02-93ER54197, by Scientific Discovery Through Advanced Computing (SciDAC) Grant No. UTA18000275, and by the Engineering and Physical Sciences Research Council (EPSRC) [EP/R034737/1]. The simulations presented in this article were performed on computational resources managed and supported by Princeton Research Computing, a consortium of groups including the Princeton Institute for Computational Science and Engineering (PICSciE) and the Office of Information Technology's High Performance Computing Center and Visualization Laboratory at Princeton University.

- [1] B. Coppi, M. N. Rosenbluth, and R. Z. Sagdeev, Instabilities due to Temperature Gradients in Complex Magnetic Field Configurations, *The Physics of Fluids* **10**, 582 (1967).
- [2] Z. Lin, T. S. Hahm, W. W. Lee, W. M. Tang, and R. B. White, Turbulent Transport Reduction by Zonal Flows: Massively Parallel Simulations, *Science* **281**, 1835 (1998),

publisher: American Association for the Advancement of Science.

- [3] A. M. Dimits, G. Bateman, M. A. Beer, B. I. Cohen, W. Dorland, G. W. Hammett, C. Kim, J. E. Kinsey, M. Kotschenreuther, A. H. Kritiz, L. L. Lao, J. Mandrekas, W. M. Nevins, S. E. Parker, A. J. Redd, D. E. Shumaker, R. Sydora, and J. Weiland, Comparisons and

- physics basis of tokamak transport models and turbulence simulations, *Physics of Plasmas* **7**, 969 (2000).
- [4] B. N. Rogers, W. Dorland, and M. Kotschenreuther, Generation and Stability of Zonal Flows in Ion-Temperature-Gradient Mode Turbulence, *Physical Review Letters* **85**, 5336 (2000).
 - [5] M. N. Rosenbluth and F. L. Hinton, Poloidal Flow Driven by Ion-Temperature-Gradient Turbulence in Tokamaks, *Physical Review Letters* **80**, 724 (1998).
 - [6] F. L. Hinton and M. N. Rosenbluth, Dynamics of axisymmetric and poloidal flows in tokamaks, *Plasma Physics and Controlled Fusion* **41**, A653 (1999).
 - [7] N. Winsor, J. L. Johnson, and J. M. Dawson, Geodesic Acoustic Waves in Hydromagnetic Systems, *The Physics of Fluids* **11**, 2448 (1968).
 - [8] G. D. Conway, A. I. Smolyakov, and T. Ido, Geodesic acoustic modes in magnetic confinement devices, *Nuclear Fusion* **62**, 013001 (2021), publisher: IOP Publishing.
 - [9] M. Barnes, F. I. Parra, and A. A. Schekochihin, Critically Balanced Ion Temperature Gradient Turbulence in Fusion Plasmas, *Physical Review Letters* **107**, 115003 (2011).
 - [10] Y.-c. Ghim, A. A. Schekochihin, A. R. Field, I. G. Abel, M. Barnes, G. Colyer, S. C. Cowley, F. I. Parra, D. Dunai, and S. Zoletnik, Experimental Signatures of Critically Balanced Turbulence in MAST, *Physical Review Letters* **110**, 145002 (2013).
 - [11] P. J. Catto, Linearized gyro-kinetics, *Plasma Physics* **20**, 719 (1978).
 - [12] M. Barnes, F. Parra, and M. Landreman, stella: An operator-split, implicit-explicit deltaf-gyrokinetic code for general magnetic field configurations, *Journal of Computational Physics* **391**, 365 (2019).
 - [13] T. E. Stringer, Diffusion in Toroidal Plasmas with Radial Electric Field, *Physical Review Letters* **22**, 770 (1969).
 - [14] A. B. Hassam and J. F. Drake, Spontaneous poloidal spin-up of tokamak plasmas: Reduced equations, physical mechanism, and sonic regimes, *Physics of Fluids B: Plasma Physics* **5**, 4022 (1993).
 - [15] K. Hallatschek and D. Biskamp, Transport Control by Coherent Zonal Flows in the Core/Edge Transitional Regime, *Physical Review Letters* **86**, 1223 (2001).
 - [16] K. Itoh, K. Hallatschek, and S.-I. Itoh, Excitation of geodesic acoustic mode in toroidal plasmas, *Plasma Physics and Controlled Fusion* **47**, 451 (2005).
 - [17] P. Goldreich and S. Sridhar, Toward a theory of interstellar turbulence. 2: Strong alfvénic turbulence, *The Astrophysical Journal* **438**, 763 (1995).
 - [18] The study by [9] also compared their scalings with gyrokinetic simulations of the Cyclone Base Case. However, due to computational limitations, the range of temperature gradients was limited to $R/L_T \leq 17.5$, where a cubic fit is a good approximation to an offset linear dependence, see Fig. 5a.
 - [19] N. Mandell, W. Dorland, and M. Landreman, Laguerre-Hermite pseudo-spectral velocity formulation of gyrokinetics, *Journal of Plasma Physics* **84**, 905840108 (2018).
 - [20] N. R. Mandell, W. Dorland, I. Abel, R. Gaur, P. Kim, M. Martin, and T. Qian, GX: a GPU-native gyrokinetic turbulence code for tokamak and stellarator design (2022), arXiv:2209.06731 [physics].
 - [21] X. Garbet, P. Mantica, F. Ryter, G. Cordey, F. Imbeaux, C. Sozzi, A. Manini, E. Asp, V. Parail, R. Wolf, and t. J. E. Contributors, Profile stiffness and global confinement, *Plasma Physics and Controlled Fusion* **46**, 1351 (2004).
 - [22] B. F. McMillan, S. Jolliet, T. M. Tran, L. Villard, A. Bottino, and P. Angelino, Avalanchelike bursts in global gyrokinetic simulations, *Physics of Plasmas* **16**, 022310 (2009).
 - [23] C. Gillot, G. Dif-Pradalier, X. Garbet, O. Panico, Y. Sarazin, R. Varennes, and D. Zarzoso, Investigation of tokamak turbulent avalanches using wave-kinetic formulation in toroidal geometry, *Journal of Plasma Physics* **87**, 905870221 (2021).
 - [24] F. Rath, A. G. Peeters, R. Buchholz, S. R. Grosshauser, P. Migliano, A. Weikl, and D. Strintzi, Comparison of gradient and flux driven gyro-kinetic turbulent transport, *Physics of Plasmas* **23**, 052309 (2016).

| κ | q | L_x/ρ_i | L_y/ρ_i | N_θ | N_x | N_y | N_μ | N_{v_\parallel} | D_h |
|----------|-----|--------------|--------------|------------|-------|-------|---------|-------------------|-------|
| 6.9 | 1.4 | 156 | 157 | 24 | 256 | 192 | 12 | 64 | 0.05 |
| 10.4 | 1.4 | 231 | 232 | 24 | 384 | 288 | 12 | 64 | 0.05 |
| 13.9 | 1.4 | 312 | 314 | 24 | 512 | 384 | 12 | 64 | 0.05 |
| 16.7 | 1.4 | 625 | 628 | 32 | 1152 | 1024 | 12 | 64 | 0.12 |
| 20.9 | 1.4 | 625 | 628 | 32 | 1152 | 1024 | 12 | 64 | 0.15 |
| 10.4 | 2.8 | 412 | 415 | 32 | 384 | 256 | 12 | 64 | 0.10 |
| 10.4 | 4.2 | 500 | 628 | 32 | 512 | 384 | 12 | 64 | 0.10 |

TABLE I: Parameters in **stella** [12] simulations.

| | L_x/ρ_i | L_y/ρ_i | N_θ | N_x | N_y | N_l | N_h | D_h |
|----------------|--------------|--------------|------------|-------|-------|-------|-------|-------|
| κ -scan | 238 | 400 | 14 | 512 | 1024 | 12 | 8 | 0.1 |
| q -scan | 318 | 533 | 14 | 512 | 1024 | 6 | 8 | 0.1 |

TABLE II: Parameters in **GX** [19, 20] simulations.

Appendix A: Gyrokinetic simulation details

All simulations presented in this Letter modelled a flux-tube extending for a single poloidal turn in the Cyclone Base Case tokamak. In addition to the parameters given in the main text, a magnetic shear of

$\hat{s} = d \ln q / d \ln r = 0.8$ was used, and the density gradient was held fixed at $R/L_n \equiv -R d \ln n_i / dr = 2.2$. A hydrogen plasma with $Z_i = 1$ was considered, and the electron to ion temperature ratio was set to $\tau = 1$.

The numerical parameters employed in the **stella** [12] gyrokinetic simulations are provided in Table I. The quantities L_x/ρ_i and L_y/ρ_i denote the box size in the radial and binormal directions, respectively, and may be related to the minimum wavenumber through $k_{\min} = 2\pi/L$. Furthermore, N_θ gives the parallel resolution, while N_x and N_y denote the number of Fourier modes in the radial and binormal directions. The velocity resolution is given by N_μ and N_{v_\parallel} for the magnetic moment and the parallel velocity, respectively, with $v_\parallel/v_{Ti} \in [-3.5, 3.5]$ for all simulations. Finally, D_h denotes the hyperdissipation parameter.

As shown in Table II, the simulations using the **GX** code [19, 20] could be run at fixed numerical parameters as κ and q were varied, as the computational cost is small owing to the use of GPUs. In the κ -scan, temperature gradient values of $\kappa \in [6.9, 13.9, 20.9, 27.8, 34.7, 41.7, 48.6]$ were considered, at fixed safety factor $q = 1.4$, while for the q -scan, $\kappa = 13.9$ and $q \in [1.4, 2.8, 4.2, 5.6, 7.0]$. The velocity resolution is here given by the number of Hermite and Laguerre moments N_h and N_l , respectively.